In vivo video-rate cellular-level full-field optical coherence tomography

Masahiro Akiba[*]
Kin Pui Chan[*]
Yamagata Promotional Organization for Industrial
    Technology
2-2-1, Matsuei
Yamagata 990-2473, Japan

Abstract. Full-field optical coherence tomography (FF-OCT) capable of *in vivo* cellular-level imaging is demonstrated for nonscanning horizontal cross-sectional imaging. The system is based on a white light interference microscope illuminated by a thermal light source. A dual-channel two-dimensional (2-D) detection technique incorporated with a pair of CCD cameras has been developed, where a pair of interferometric images with phase difference of $\pi/2$ are simultaneously captured using an achromatic phase shifter. By acquiring an additional pair of images with a conventional phase shift method, a horizontal cross section is derived from every two consecutive CCD frames, enabling OCT imaging at the video rate. Using an ultrabroad bandwidth illumination incorporated with relatively high NA (0.8 NA) water immersion objectives, an axial resolution of 0.8 μm and a transverse resolution of 0.7 μm are experimentally confirmed. A field of view of 215 μm $\times$ 215 μm is covered by the 500 $\times$ 500 pixel CCD cameras. We demonstrate, for what is believed to be the first time, *in vivo* cellular-level blood flow imaging of a *Xenopus laevis* tadpole by FF-OCT. © *2007 Society of Photo-Optical Instrumentation Engineers.*
 [DOI: 10.1117/1.2822159]

Keywords: optical coherence tomography (OCT); full-field; ultrahigh resolution; video rate; cellular-level imaging; blood flow imaging.

Paper 07133R received Apr. 7, 2007; revised manuscript received Jun. 6, 2007; accepted for publication Jun. 27, 2007; published online Dec. 28, 2007.

1 Introduction

Optical coherence tomography (OCT) is an emerging bio-medical optical imaging technique that can perform high-resolution, cross-sectional imaging in biological tissues.[1,2] OCT was first applied in ophthalmology for *in vivo* retinal imaging[3,4] and has proven to be useful for the diagnosis of macular and optic disk diseases.[5,6] Ultrahigh resolution OCT has also been demonstrated for cellular imaging using a state-of-the-art femtosecond laser or supercontinium light source.[7–10] In recent years, the progress of OCT technology utilizing a spectrometer-based OCT or swept-source-based OCT has gained much attention in ophthalmology[11–17] and other biological tissue imaging.[18,19]

Full-field optical coherence tomography (FF-OCT)[20–22] is known as a nonscanning approach to OCT, where the detected horizontal cross-sectional image is of the same form as that obtained in the *en face*[23] or transverse scanning OCT.[24] FF-OCT is based on an interference microscope, where a parallel beam is illuminated to the sample and the backscattered light is detected using a two-dimensional (2-D) sensor array (e.g., CCD or CMOS camera). The sectioning capability (axial resolution) of FF-OCT is determined by the coherence length of the light source, while the transverse resolution is mainly

determined by the magnification of the imaging system. Since the light source is employed to illuminate the sample, a spatially incoherent light source such as a halogen lamp or xenon arc lamp is well suited in FF-OCT to achieve both high axial and high transverse resolutions. The use of a spatially incoherent source also offers the advantage of cross-talk suppression.[25]

An FF-OCT system using a thermal light source has been demonstrated by Vabre et al. for ultrahigh ($\sim$1 μm) resolution imaging.[26] A three-dimensional (3-D) image of a *Xenopus laevis* tadpole was reconstructed using a stack of FF-OCT images with unprecedented resolutions. However, the reported imaging speed is relatively slow ($\sim$1 s per image), due to the practical requirement of image averaging to improve the detection sensitivity. Recently, Grieve et al. have developed a rapid FF-OCT system associated with a high-speed CMOS camera, enabling *in vivo* anterior segment imaging of small animals.[27] More recently, Moneron et al. have developed a stroboscopic FF-OCT system, in which image acquisition time has been dramatically reduced to $\sim$10 μs by using a xenon flash lamp and a pair of CCD cameras.[28] FF-OCT has been expected for high-resolution 3-D imaging, in which the images acquired are comparable to those of confocal microscopy.[29,30]

So far we have developed a video-rate FF-OCT imaging system using a dual-channel parallel heterodyne detection technique with a pair of CCD cameras.[31] Three-dimensional

---

[*]Current address: TOPCON Advanced Biomedical Imaging Laboratory, 53 West Century Road, Paramus, New Jersey 07652.
Address all correspondence to Masahiro Akiba, TOPCON Advanced Biomedical Imaging Laboratory, 53 West Century Road, Paramus, NJ 07652; Tel: 201–599–5237; fax: 201–599–5260 E-mail: makiba@topcon.com
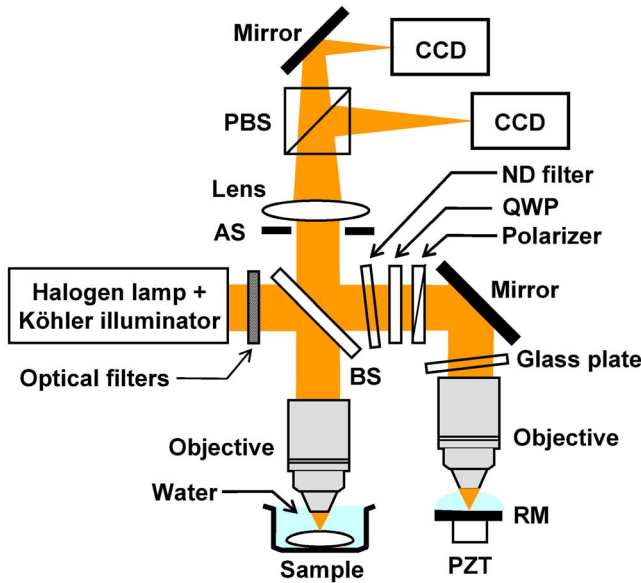
Fig. 1 Ultrahigh-resolution FF-OCT system based on a white light interference microscope using a dual-channel detection technique. BS: beamsplitter; QWP: quarter wave plate; RM: reference mirror; PZT: piezoelectric transducer; AS: aperture stop; PBS: polarization beamsplitter.

imaging was performed in a single longitudinal scan, making 100 frames/s imaging possible. However, the strict requirement of frequency stability in synchronous detection is apparently a drawback for an *in vivo* imaging application. Sample motion may adversely affect the frequency stability, lowering the signal-to-noise ratio (SNR). Recently, we have built an ultra-high-resolution FF-OCT system using a thermal light source and a CCD camera. Investigations of the ocular tissue structure of a donor cornea and a porcine eye at the subcellular level have been carried out.[32,33] In this setup, however, a phase-shift-based detection technique was employed, and the measurement time was relatively lengthy, making it difficult for real-time imaging. In this paper, we describe a novel dual-channel FF-OCT system for ultrahigh-resolution and high-speed imaging. We demonstrate what is to our best knowledge the first *in vivo* video-rate cellular-level imaging result of blood cell dynamics of a *Xenopus laevis* tadpole by FF-OCT.

2 Experimental Setup

2.1 Hardware Configuration

A schematic of our FF-OCT system is shown in Fig. 1. The system is based on a white light interference microscope with a Linnik-type configuration. The radiation from a 150-W tungsten halogen lamp is incidented into a flexible fiber bundle (not shown), and it is conducted to a Köhler illumination (KI) system that consists of four aspheric lenses and two variable apertures. The KI system is intended to be used for a uniform illumination to the sample, as in a conventional microscope. The output quasi-parallel beam from the KI system is launched into the Michelson interferometer and then split into the signal and reference beams by a 50:50 beamsplitter. Two identical infinity-corrected water immersion microscope objectives (40×, 0.8 NA, LUMPLFL40XW/IR2, Olympus,

Tokyo) with a working distance of 3.4 mm are placed in both arms of the interferometer. An achromatic quarter wave plate (QWP) and a linear polarizer are inserted in the reference arm. The light beam reflected back by a reference mirror is again passed through the linear polarizer and the QWP so that the light beam returning to the BS becomes a circularly polarized light. A drop of water (W3500 cell cultured water, Sigma-Ardorich, St. Louis, Missouri) is placed as an immersion fluid between the tip of the objective and the total reflection mirror. A neutral density (ND) filter whose transmittance is experimentally optimized to 13% is set in the reference arm to increase the visibility of the interferometric image. On the other hand, the sample is illuminated with a randomly polarized light. To compensate for a residual dispersion mismatch between the signal and the reference arms, a BK7 glass plate is placed in the reference arm so that the dispersion is initially matched. The recombined output beam from the interferometer is detected by the microscope setup, where the interference light is divided into two orthogonal parts by a polarization beamsplitter (PBS) before reaching the two identical CCD cameras (MC-512PF, Texas Instruments, Tokyo). The CCD cameras employed have 500×500 pixels with a 12-bit resolution at an output rate of 30 Hz.

Provided that the sample exhibits no birefringence, the dual CCD outputs exhibit a phase difference of $\pi/2$ and can be expressed as follows:

$$C_{A1}(x,y) = I_s(x,y) + I_r(x,y) + I_{inc}(x,y)$$
$$+ \alpha[I_s(x,y)I_r(x,y)]^{1/2} \cos[\phi(x,y)], \quad (1)$$

$$C_{B1}(x,y) = I_s(x,y) + I_r(x,y) + I_{inc}(x,y)$$
$$+ \alpha[I_s(x,y)I_r(x,y)]^{1/2} \sin[\phi(x,y)], \quad (2)$$

where $I_s(x,y)$ and $I_r(x,y)$ are the signal and reference intensities, respectively, $I_{inc}(x,y)$ is a backscattering component that does not contribute to the interference signal, $\phi(x,y)$ is an initial phase difference between the signal and the reference lights, and α is a numerical factor. The dual CCD outputs contain a common background of $I_s(x,y) + I_r(x,y) + I_{inc}(x,y)$, while their respective interferometric terms $\alpha[I_s(x,y)I_r(x,y)]^{1/2} \cos[\phi(x,y)]$ and $\alpha[I_s(x,y)I_r(x,y)]^{1/2} \sin[\phi(x,y)]$ correspond to the sine and cosine components.

To extract the sine and cosine components from the CCD outputs, a subtraction of the background component is needed. In the present setup, we measure an additional pair of images $C_{A2}(x,y)$ and $C_{B2}(x,y)$ with a phase shift of π by using a piezoelectric transducer (PZT) that is glued to the reference mirror. An FF-OCT image is then derived by summing the squares of the sine and cosine components of the interference signal as follows:

$$[C_{A1}(x,y) - C_{A2}(x,y)]^2 + \gamma[C_{B1}(x,y) - C_{B2}(x,y)]^2$$
$$= 4\alpha^2 I_s(x,y)I_r(x,y) \propto I_s(x,y), \quad (3)$$

where γ is a numerical factor determined by the ratio of the amount of light intensity incident on the CCD cameras. The value of γ is measured in advance before the experiment. In this manner, two consecutive frames are recorded to derive a
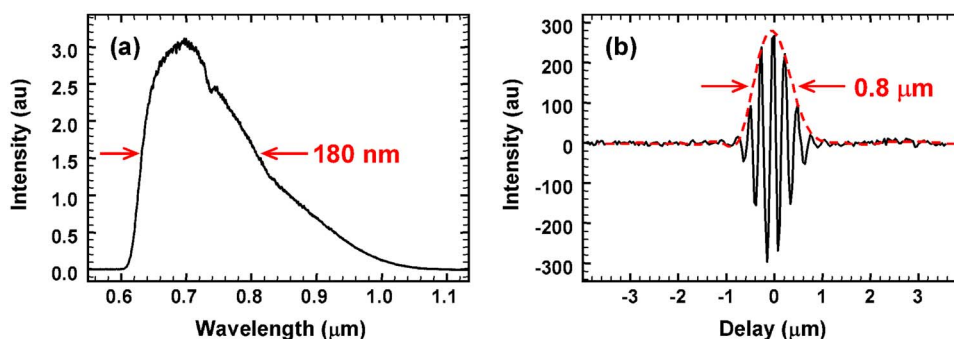
Fig. 2 (a) Spectrum of the filtered output of a halogen lamp employed for FF-OCT imaging, and (b) the axial response profile of one pixel measured by scanning a total reflection mirror along the optical axis.

single FF-OCT image. The FF-OCT image is displayed using a logarithmic lookup table with a 256 gray scale, where a high reflectance is displayed as white against a black background. It is noteworthy that the frame subtraction in the present setup offers the advantage that the fixed pattern noise in the CCD camera can be removed when two consecutive frames with a phase difference of π are subtracted. Functionally, the detected four frames in the present system are equivalent to those acquired in the previously reported four-frame phase shift detection scheme.[32]

To synchronize the dual-detection channels, common pulse signals are applied to the CCD cameras through a programmable camera control line in the camera link format. The alternative voltage changes applied to the PZT, which correspond to phase shifts of 0 and π, are triggered by the frame-sync signal from one CCD camera so that every two consecutive CCD frames exhibit a relative phase difference of π in the interference image.

The validity of Eq. (3) requires that the two CCD cameras capture exactly the same field. In other words, a pixel-to-pixel correspondence between the CCD cameras is needed. Mechanically, one camera is stationary, while the other camera that is mounted on a xyz translation stage is manually aligned to its counterpart with a subpixel accuracy. The alignment employs either home-written template matching or image-correlation software. This calibration is done once in the initial setting of the system.

2.2 Image Acquisition Software

We wrote a software program that performs three main functions: monitor mode for real-time observation, time-lapse mode for 2-D video-rate imaging, and z-stack mode for 3-D imaging. In monitor mode, a software sequence including image acquisition, processing, and display is repeated at a 5-Hz rate. Second, in time-lapse mode, FF-OCT images are continuously detected at a fixed depth as a function of time to achieve a time-sequence image. Assuming that the consecutive frames with a phase difference of π are C_1, C_2, $C_3, \ldots, C_{n-1}$, and C_n, the frame subtractions of $C_1 - C_2$, $C_2 - C_3, \ldots, C_{n-1} - C_n$ may effectively remove the background component to derive the sequential FF-OCT images using Eq. (3). Using such a rolling manner, video-rate (30 frames/s) imaging is made possible. To avoid the possible fringe averaging during *in vivo* imaging, the exposure time of the cameras is set to 6.4 ms, while the frame interval is fixed at 33 ms

so that a single FF-OCT image can be acquired as short as 40 ms. Third, in z-stack mode, the sample is placed in a motorized z-translation stage (ALV-600-H0M, Chuo Precision Industrial, Tokyo) and is translated along the optical axis to yield a stack of FF-OCT images. In this mode, the exposure time is set to 33 ms. Using such a 3-D data set, a longitudinal cross section (xz- or yz-), which is of the common form of the conventional OCT tomogram, can be sectioned out by software. Illumination flux is also adjusted so that the camera pixels are close to the saturation level in both imaging modes.

2.3 Basic Performance

Although a half-micron axial resolution can be achieved by fully exploiting the extremely broad bandwidth of the halogen lamp, only a partial band in the near infrared ranging from 600 nm to 1000 nm has been chosen. Optical filters are inserted at the exit of the KI system to cut off the visible and long wavelength components. To avoid any thermal injuries of the sample, a short pass filter (passband of <1.1 μm) is inserted as well. This wavelength region has been chosen by considering the weaker absorption and better penetration in most of the biological tissues, and also the wavelength dependency of the polarization optics employed. To reduce unwanted reflections, all optical components are antireflection coated for the wavelength range employed. The resultant spectrum is shown in Fig. 2(a). The spectrum was measured at the exit of the interferometer by blocking the sample arm so that it contains a transmittance dependency of the overall optics. In the present study, a spectrally filtered source having a full-width at half maximum (FWHM) of 180 nm centered around 700 nm was employed, yielding a theoretical axial resolution of 0.9 μm in water. It should be noted that the effective spectrum for imaging is a product of the source spectrum and the spectral response of the CCD chip. Figure 2(b) shows the axial response profile of one pixel measured by scanning a total reflection mirror along the optical axis. As seen in Fig. 2(b), the axial point spread function detected by FF-OCT exhibits a symmetrical form, with negligible side-lobes. The measured value of 0.8 μm (FWHM) is slightly better than the theoretical value, mainly because the spectrum is slightly different from the Gaussian distribution.

The theoretical transverse resolution (Δx, Δy) is determined by the well-known formula $\Delta x = 0.66\lambda/\mathrm{NA}$. An 0.8-NA objective employed yields $\Delta x = \Delta y = 0.58$ μm at the

wavelength of $\lambda = 700$ nm, while we experimentally confirmed a transverse resolution of 0.7 μm using the edge response (10 to 90%) of a silicon wafer as a sample. In tissue imaging, however, aberration may degrade the transverse resolution when imaging at a deeper position due to multiple scattering.

The theoretical detection sensitivity for FF-OCT is described in the literature.[20,34] We followed the equation by considering a four-frame phase shift detection technique. A full-well capacity of the camera is an important factor to achieve a high sensitivity measurement. The CCD camera employed has a full-well capacity of 400,000 electrons, and the theoretical detection sensitivity is calculated to be ~80 dB. The measured detection sensitivity was approximately 75 dB. Unwanted back-reflection from the optical components in the FF-OCT setup and an uneven ploarization splitting ratio by the PBS may account for a sensitivity loss.

A typical FF-OCT image acquired by our system consists of 500×500 pixels covering an area of 215 μm $\times$ 215 μm. The illumination flux to the biological tissue is approximately 3 mW/mm^2. In the measerement, where the exposure time of the CCDs was shortened to 6.4 ms, the incident power was adequetely increased.

2.4 Sample Preparation

A *Xenopus laevis* (African frog) tadpole of stage 40 to 45 was chosen for the present study. *Xenopus laevis* is a widely used and well-characterized developmental biology animal model and is commonly used in OCT measurement to demonstrate the visualization of the morphological structure[35–38] as well as the cardiovascular activity.[39,40]

Xenopus laevis tadpoles were bred in an aquarium tank at 23 to 25°C until measurements were performed. The first group of specimens were anesthetized by immersion in diluted ketamine solution for 10 min until they no longer responded to touch. The second group of specimens were fixed in 4% buffered solution of formaldehyde for an hour until no cardiac activity was observed. The tadpoles were transferred to a Petri dish and then submerged in water at room temperature. Specimens were oriented for imaging with the optical beam incident from either the dorsal or ventral sides. No staining and contrast agents were used. All animal handling was performed according to protocols approved by the Committee on Animal Care, Yamagata Promotional Organization for Industrial Technology.

3 Results

3.1 Time-Lapse Imaging

To demonstrate the video-rate imaging capability of our FF-OCT system, Fig. 3 shows examples of the FF-OCT images of an anesthetized tadpole at approximately 0.3-s time interval. Figures 3(a) and 3(d) are detected where the speed of the blood flow is minimum. It can be seen from these images that individual blood cells are visible as well as the cellular structure of the tadpole. Time-lapse imaging results can be seen in Video 1. The movie shows a total of 300 FF-OCT images recorded during a period of 10 s. Outputs from the CCD cameras were continuously captured and stored in the computer main memory for post-processing. FF-OCT imaging was per-
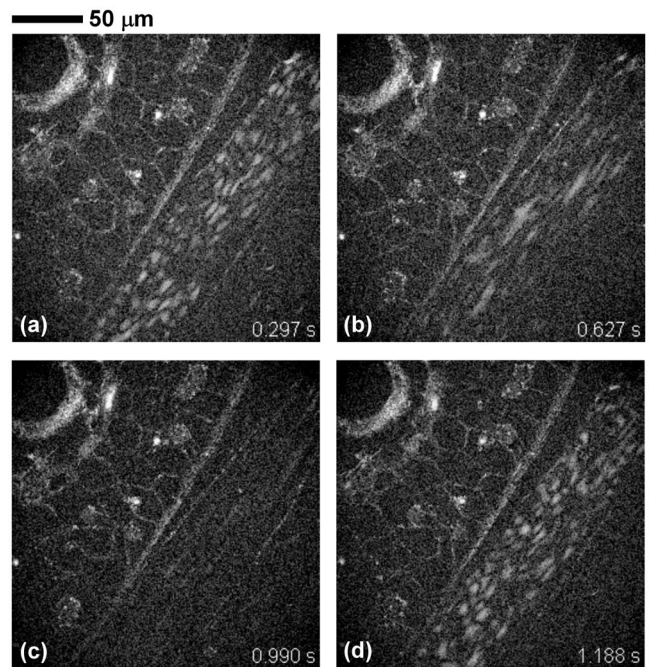

Fig. 3 (a) to (d): Examples of time-lapse FF-OCT imaging results of an anesthetized tadpole recorded at a video rate. Images are selected at approximately 0.3-s time intervals. A movie clip can be seen in Video 1. The image size in the movie clip is half size to reduce the file size.

formed with the tadpole ventral side up, and the time-lapsed images were taken near the exit of the aorta. In the movie, the pulsatile blood cells are clearly visualized. It is noteworthy that both the cell nuclei and the blood flow can be observed in a single image, where the expansion and contraction of a blood vessel can be seen in accordance with a pulsation of the blood flow. It is estimated from the movie clip that the pulsation occurs at a rate of 2.2 Hz. The 30 frames/s imaging speed and the ultrahigh spatial resolution of our system make it possible to identify most of the individual blood cells during diastole of the heart. During systole, however, the blood cells move beyond the temporal resolution of the present system,
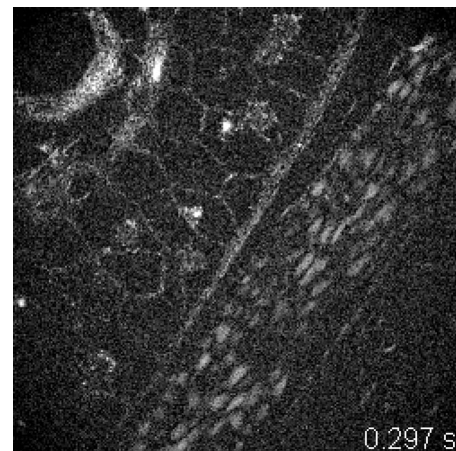
Video 1 Time-lapse imaging results recorded during a period of 10 s (AVI, 5.7 MB). [URL: http://dx.doi.org/10.1117/1.2822159.1]
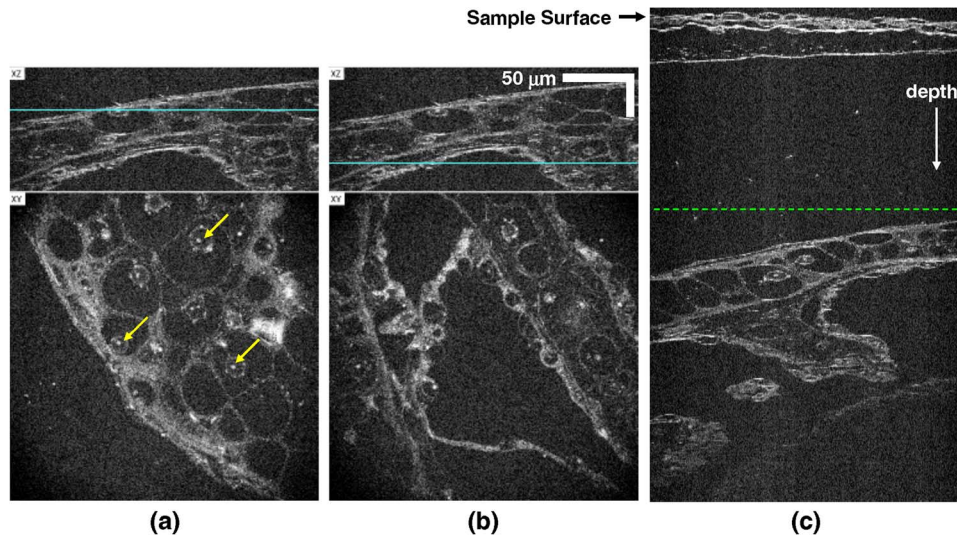
Fig. 4 OCT images of a fixed tadpole. The lower parts of (a) and (b) depict the FF-OCT images measured at different depths, while the upper parts show the longitudinal cross sections reconstructed from the z-stack imaging. A movie clip can be seen in Video 2. The image size of the movie clip is half size to reduce the file size. For reference, (c) depicts a longitudinal cross section, where the broken line indicates the initial depth from which the z-stack measurement was started.

so that the images of blood cells appear to be blurred [Fig. 3(b)] and, in the severe case, averaged out [Fig. 3(c)].
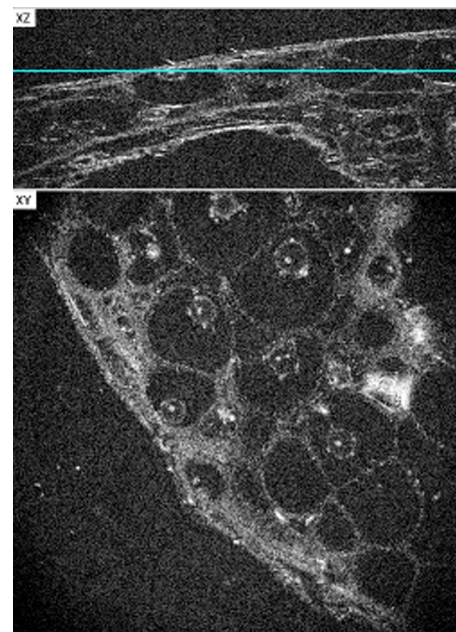
3.2 Z-Stack Imaging

In the feasibility study of FF-OCT for ultrahigh-resolution 3-D morphological imaging, a series of FF-OCT images was acquired from the dorsal side to the ventral side of a fixed tadpole with a depth interval of 0.75 μm. Four FF-OCT images were averaged at each depth position to increase the image contrast, and the measurement of 3-D volume involving FF-OCT imaging at 200 depths took approximately 70 s. The lower parts of Figs. 4(a) and 4(b) show the representative FF-OCT images at different depths of 300 μm and 370 μm, respectively, while the upper parts of (a) and (b) depict the longitudinal cross section reconstructed from the 3-D OCT volume. The cyan line indicates the depth where the FF-OCT image shown in the lower part of the figure was measured. Z-stack imaging results can be seen in Video 2.

Features of the internal architectural morphology, such as cell membranes, boundaries of the cell cytoplasm, and cell nuclei, are distinctly visible from the FF-OCT images. It is interesting to note that inside the cell nuclei, a bright spot is always observed. Such bright spots at the individual cells are indicated by arrows in Fig. 4(a). These bright spots might correspond to the nucleolus, and the fine fibers connected to the cell membrane might correspond to the cytoskeleton. A similar structure has also been reported in Ref. 38. Identification of the details of the other complicated internal morphology are under investigation. It can be seen from the movie clip that FF-OCT provides enriched information about cellular structure along the horizontal plane.

It is noteworthy that the present z-stack imaging started from a depth approximately 250 μm below the sample surface. A longer-range yet more time consuming z-scan [Fig. 4(c)] reveals that the OCT images shown in Figs. 4(a) and 4(b) reflect the details of a second layer under the sample

surface. In Fig. 4(c), the broken line indicates the initial measurement depth of the z-scans in Figs. 4(a) and 4(b). The results in Figs. 3 and 4 show some of the advantages of the present FF-OCT scheme over conventional OCT. FF-OCT is a nonscanning method capable of capturing an ultrahigh-resolution horizontal cross-sectional image that is constantly matched to the focal plane. Video-rate FF-OCT imaging offers the opportunity of continuous (time-lapsed) observation of cellular dynamics at a fixed depth. While speckles are prominent in conventional OCT and adversely affect the im-

age contrast, they are minimal in Figs. 3 and 4, demonstrating another advantage of FF-OCT using a spatially incoherent thermal source.

4 Discussion and Conclusions

An FF-OCT system using a newly developed dual-channel detection scheme has been applied to *in vivo* imaging at a cellular level. Although we have demonstrated the visualization of individual flowing blood cells in the vessel, further improvement in the imaging speed that permits the visualization of faster flowing individuals may yield practical applications in biomedical diagnosis. The imaging speed of the present system is primary limited by the CCD frame rate. To avoid motion artifact and the resultant fringe averaging, the exposure time of the camera has been set to 6.4 ms, despite of a frame interval of 33 ms. Obviously, the "on-off" duty ratio of the CCD camera is merely 1:5. Therefore, the use of a CCD camera with five times higher frame rate may yield up to five times higher imaging speed without compromising the exposure time. The development of a higher-speed FF-OCT system using high-speed CCD cameras is underway in our laboratory.

In our detection method, the sine and cosine components of the interference signal are extracted to form a FF-OCT image. Although a more straightforward method to obtain the signal intensity by differentiating two phase-opposed interference images has been reported by Moneron et al.,[28] the uncertainty factor of $\cos^2(\phi)$, where ϕ is an initial phase between signal and reference lights, could be multiplied to the final OCT image, making the FF-OCT image low contrast and fluctuating point by point. As such, the present detection scheme offers a practical advantage of imaging stability in biological tissue imaging.

The depth of focus (DOF), which is also recognized as a confocal parameter, is inversely proportional to the NA of the objective, $DOF=(2\lambda)/(\pi NA^2)$. Using an objective with 0.8 NA and $\lambda=700$ nm, it is calculated that $DOF=0.7$ μm, which is nearly equal to the OCT axial resolution given by the coherence length. In FF-OCT imaging, an optimal sensitivity is achieved when the coherence-gated detection plane is matched to the focal plane of the microscope. Therefore, care must be taken to maintain a matching between the two planes when imaging at a deeper position. In tissue imaging, however, the mismatch of refractive indexes of the tissue sample and water may cause the focal plane to move away from the coherence-gated plane, so the sensitivity could be significantly degraded. As a solution, dynamic focusing techniques have been proposed.[41,42] In our measurement, the average refractive index of the *Xenopus* specimen, which is assumed to be 1.35 according to Tearney et al.,[43] is close to that of water (1.33). Therefore, dynamic focusing has not been applied to our water immersion FF-OCT system.

In the presence of birefrigence in the tissue sample, the intensities of the two orthogonal parts of the backscattering light will become uneven, yielding an undesired image artifact in the present detection scheme. Meanwhile, the scattering of light is a dominant factor that limits the imaging depth of OCT. The $\sim$20-dB lower sensitivity of FF-OCT as compared to the conventional (longitudinal) OCT may limit its application to a lesser depth. However, it has been demon-strated in the present work that ultrahigh-resolution FF-OCT is capable of providing enriched information about the morphological structure at a cellular level. Since scattering is less severe at a longer wavelength, FF-OCT system operated at the longer wavelength may have the advantage of deeper penetration. For this purpose, InGaAs CCD cameras sensitive at 1.3 μm and beyond can be employed for FF-OCT imaging.[34,37,42]

In conclusion, we have developed an ultrahigh-resolution FF-OCT system using a low-cost thermal light source incorporated with a pair of CCD cameras. The system has been applied to *in vivo* imaging of living specimens and demonstrated to be capable of visualizing the individual cells, including blood cell dynamics. With a spatial resolution of $\sim$1 μm $\times$ $\sim$1 μm $\times$ $\sim$1 μm, the present system may be further developed for the use as an "optical histology," and it may potentially contribute to investigations of developmental biology and cell interaction as well. The use of a contrast-enhanced material such as microspheres to change the scattering characteristics and to label a single cell may also allow the identification of cells and lead to functional cellular imaging *in vivo*.

References

1. D. Huang, E. A. Swanson, C. P. Lin, J. S. Schuman, W. G. Stinson, W. Chang, M. R. Hee, T. Flotte, K. Gregory, C. A. Puliafito, and J. G. Fujimoto, "Optical coherence tomography," *Science* **254**, 1178–1181 (1991).
2. J. G. Fujimoto, "Optical coherence tomography for ultrahig resolution *in vivo* imaging," *Nat. Biotechnol.* **21**, 1361–1367 (2003).
3. E. A. Swanson, J. A. Izatt, M. R. Hee, D. Huang, C. P. Lin, J. S. Schuman, C. A. Puliafito, and J. G. Fujimoto, "*In vivo* retinal imaging by optical coherence tomography," *Opt. Lett.* **18**, 1864–1866 (1993).
4. W. Drexler, U. Morgner, R. K. Ghanta, F. X. Kartner, J. S. Schuman, and J. G. Fujimoto, "Ultrahigh-resolution ophthalmic optical coherence tomography," *Nat. Med.* **7**, 502–507 (2001).
5. T. H. Ko, J. G. Fujimoto, J. S. Duker, L. A. Paunescu, W. Drexler, C. R. Baumal, C. A. Puliafito, E. Reichel, A. H. Rogers, and J. S. Schuman, "Comparison of ultrahigh- and standard-resolution optical coherence tomography for imaging macular hole pathology and repair," *Ophthalmology* **111**, 2033–2043 (2004).
6. J. S. Schuman, C. A. Puliafito, and J. G. Fujimoto, Eds., *Optical Coherence Tomography of Ocular Diseases*, 2nd ed., Slack, Inc., Thorofare, NJ (2004).
7. W. Drexler, U. Morgner, F. X. Kartner, C. Pitris, S. A. Boppart, X. D. Li, E. P. Ippen, and J. G. Fujimoto, "*In vivo* ultrahig-resolution optical coherence tomography," *Opt. Lett.* **24**, 1221–1223 (1999).
8. S. Boppart, B. E. Bouma, C. Pitris, J. F. Southern, M. E. Brezinski, and J. G. Fujimoto, "*In vivo* cellular optical coherence tomography imaging," *Nat. Med.* **4**, 861–864 (1998).
9. B. Povazay, K. Bizheva, A. Unterhuber, B. Hermann, H. Sattmann, A. F. Fercher, W. Drexler, A. Apolonski, W. J. Wadsworth, J. C. Knight, P. S. J. Russell, M. Vetterlein, and E. Scherzer, "Submicrometer axial resolution optical coherence tomography," *Opt. Lett.* **27**, 1800–1802 (2002).
10. Y. Wang, Y. Zhao, J. S. Nelson, Z. Chen, and R. S. Windeler, "Ultrahigh-resolution optical coherence tomography by broadband continuum generation from a photonic crystal fiber," *Opt. Lett.* **28**, 182–184 (2003).

11. M. Wojtkowski, V. Srinivasan, J. G. Fujimoto, T. Ko, J. S. Schuman, A. Kowalczyk, and J. S. Duker, "Three-dimensional retinal imaging with high-speed ultrahigh-resolution optical coherence tomography," *Ophthalmology* **112**, 1734–1746 (2005).

12. M. Choma, K. Hsu, and J. A. Izatt, "Swept source optical coherence tomography using an all-fiber 1300-nm ring laser source," *J. Biomed. Opt.* **10**, 044009 (2005).

13. R. Zawadzki, S. Jones, S. Olivier, M. Zhao, B. Bower, J. Izatt, S. Choi, S. Laut, and J. Werner, "Adaptive-optics optical coherence tomography for high-resolution and high-speed 3-D retinal *in vivo* imaging," *Opt. Express* **13**, 8532–8546 (2005).

14. T. C. Chen, B. Cense, M. C. Pierce, N. Nassif, B. H. Park, S. H. Yun, B. R. White, B. E. Bouma, G. J. Tearney, and J. F. de Boer, "Spectral domain optical coherence tomography: ultra-high speed, ultra-high resolution ophthalmic imaging," *Arch. Ophthalmol. (Chicago)* **123**, 1715–1720 (2005).

15. Y. Yasuno, V. D. Madjarova, S. Makita, M. Akiba, A. Morosawa, C. Chong, T. Sakai, K. P. Chan, M. Itoh, and T. Yatagai, "Three-dimensional and high-speed swept-source optical coherence tomography for *in vivo* investigation of human anterior eye segments," *Opt. Express* **13**, 10652–10664 (2005).

16. H. Lim, M. Mujat, C. Kerbage, E. C. Lee, Y. Chen, T. C. Chen, and J. F. de Boer, "High-speed imaging of human retina *in vivo* with swept-source optical coherence tomography," *Opt. Express* **14**, 12902–12908 (2006).

17. J. Zhang, Q. Wang, B. Rao, Z. Chen, and K. Hsu, "Swept laser source at 1 μm for Fourier domain optical coherence tomography," *Appl. Phys. Lett.* **89**, 073901 (2006).

18. S. Yun, G. Tearney, J. de Boer, N. Iftimia, and B. Bouma, "High-speed optical frequency-domain imaging," *Opt. Express* **11**, 2953–2963 (2003).

19. R. Huber, M. Wojtkowski, J. G. Fujimoto, J. Y. Jiang, and A. E. Cable, "Three-dimensional and C-mode OCT imaging with a compact, frequency swept laser source at 1300 nm," *Opt. Express* **13**, 10523–10538 (2005).

20. A. Dubois, K. Grieve, G. Moneron, R. Lecaque, L. Vabre, and C. Boccara, "Ultrahigh-resolution full-field optical coherence tomography," *Appl. Opt.* **43**, 2874–2883 (2004).

21. A. Dubois, G. Moneron, K. Grieve, and A. C. Boccara, "Three-dimensional cellular-level imaging using full-field optical coherence tomography," *Phys. Med. Biol.* **49**, 1227–1234 (2004).

22. K. Grieve, M. Paques, A. Dubois, J. Sahel, A. C. Boccara, and J.-F. Le Gargasson, "Ocular tissue imaging using ultrahigh resolution full-field optical coherence tomography," *Invest. Ophthalmol. Visual Sci.* **45**, 4126–4131 (2004).

23. R. G. Cucu, A. G. Podoleanu, J. A. Rogers, J. Pedro, and R. B. Rosen, "Combined confocal/*en face* T-scan-based ultrahigh-resolution optical coherence tomography *in vivo* retinal imaging," *Opt. Lett.* **31**, 1684–1686 (2006).

24. M. Pircher, B. Baumann, E. Gotzinger, and C. K. Hitzenberger, "Retinal cone mosaic imaged with transverse scanning optical coherence tomography," *Opt. Lett.* **31**, 1821–1823 (2006).

25. B. Karamata, P. Lambelet, M. Laubscher, R. P. Salathe, and T. Lasser, "Spatially incoherent illumination as a mechanism for cross-talk suppression in wide-field optical coherence tomography," *Opt. Lett.* **29**, 736–738 (2004).

26. L. Vabre, A. Dubois, and A. C. Boccara, "Thermal-light full-field optical coherence tomography," *Opt. Lett.* **27**, 530–532 (2002).

27. K. Grieve, A. Dubois, M. Simonutti, M. Paques, J. Sahel, J.-F. Le Gargasson, and C. Boccara, "*In vivo* anterior segment imaging in the rat eye with high speed white light full-field optical coherence tomography," *Opt. Express* **13**, 6286–6295 (2005).

28. G. Moneron, A. C. Boccara, and A. Dubois, "Stroboscopic ultrahigh-resolution full-field optical coherence tomography," *Opt. Lett.* **30**, 1351–1353 (2005).

29. M. Rajadhyaksha, R. R. Anderson, and R. H. Webb, "Video-rate confocal scanning laser microscope for imaging human tissues *in vivo*," *Appl. Opt.* **38**, 2105–2115 (1999).

30. S. J. Kolker, U. Tajcheman, and D. L. Weeks, "Confocal imaging of early heart development in *Xenopus laevis*," *Dev. Biol.* **218**, 64–73 (2000).

31. M. Akiba, K. P. Chan, and N. Tanno, "Full-field optical coherence tomography by two-dimensional heterodyne detection with a pair of CCD cameras," *Opt. Lett.* **28**, 816–818 (2003).

32. M. Akiba, N. Maeda, K. Yumikake, T. Soma, K. Nishida, Y. Tano, and K. P. Chan, "Ultrahigh resolution imaging of human donor cornea using full-field optical coherence tomography," *J. Biomed. Opt.* **12**, 041202 (2007).

33. M. Hangai, M. Akiba, K. P. Chan, Y. Fukuma, and N. Yoshimura, "Retinal ganglion cell imaging by ultrahigh resolution, full-field optical coherence tomography in pig eyes," *Invest. Ophthalmol. Visual Sci.* **47**, E-Abstract 3373 (2006).

34. Y. Watanabe, K. Yamada, and M. Sato, "*In vivo* non-mechanical scanning grating-generated optical coherence tomography using an InGaAs digital camera," *Opt. Commun.* **261**, 376–380 (2006).

35. S. A. Boppart, G. J. Tearney, B. E. Bouma, M. E. Brezinski, J. F. Southern, and J. G. Fujimoto, "Noninvasive assessment of the developing *xenopus* cardiovascular system using optical coherence tomography," *Proc. Natl. Acad. Sci. U.S.A.* **94**, 4256–4261 (1997).

36. A. D. Aguirre, P. Hsiung, T. H. Ko, I. Hartl, and J. G. Fujimoto, "High-resolution optical coherence microscopy for high-speed, *in vivo* cellular imaging," *Opt. Lett.* **28**, 2064–2066 (2003).

37. W. Y. Oh, B. E. Bouma, N. Iftimia, S. H. Yun, R. Yelin, and G. J. Tearney, "Ultrahigh-resolution full-field optical coherence microscopy using InGaAs camera," *Opt. Express* **14**, 726–735 (2006).

38. S. W. Huang, A. D. Aguirre, R. A. Huber, D. C. Adler, and J. G. Fujimoto, "Swept source optical coherence microscopy using a Fourier domain mode-locked laser," *Opt. Express* **15**, 6210–6217 (2007).

39. A. Rollins, S. Yazdanfar, M. Kulkarni, R. Ung-Arunyawee, and J. Izatt, "*In vivo* video rate optical coherence tomography," *Opt. Express* **3**, 219–229 (1998).

40. V. X. D. Yang, M. Gordon, E. Seng-Yue, S. Lo, B. Qi, J. Pekar, A. Mok, B. Wilson, and I. Vitkin, "High speed, wide velocity dynamic range Doppler optical coherence tomography (part II): imaging *in vivo* cardiac dynamics of *Xenopus laevis*," *Opt. Express* **11**, 1650–1658 (2003).

41. Y. Watanabe, Y. Hayasaka, M. Sato, and N. Tanno, "Full-field optical coherence tomography by achromatic phase shifting with a rotating polarizer," *Appl. Opt.* **44**, 1387–1392 (2005).

42. A. Dubois, G. Monerona, and Claude Boccara, "Thermal-light full-field optical coherence tomography in the 1.2 μm wavelength region," *Opt. Commun.* **266**, 738–743 (2006).

43. G. J. Tearney, M. E. Brezinski, J. F. Southern, B. E. Bouma, M. R. Hee, and J. G. Fujimoto, "Determination of the refractive index of highly scattering human tissue by optical coherence tomography," *Opt. Lett.* **20**, 2258–2260 (1995).